

Surfactant effects in the morphology and the photocatalytic activity of the BaMoO₄ crystals

Amanda Fernandes Gouveia^{1,2+id}, Gustavo Venancio Bellucci^{3id}, Lara Kelly Ribeiro^{3id}, Marcelo Assis^{3id}, Ieda Lúcia Viana Rosa^{3id}, Elson Longo^{3id}, Juan Andrés^{1id}, Miguel Angel San-Miguel^{2id}

1. University Jaume I, Department of Physical and Analytical Chemistry, Castelló, Spain.
2. State University of Campinas, Institute of Chemistry, Campinas, Brazil.
3. Federal University of Sao Carlos, Center for the Development of Functional Materials, São Carlos, Brazil.

+Corresponding author: Amanda Fernandes Gouveia, **Phone:** +34 964728071, **Email address:** gouveiad@uji.es

ARTICLE INFO

Article history:

Received: July 27, 2021

Accepted: November 09, 2021

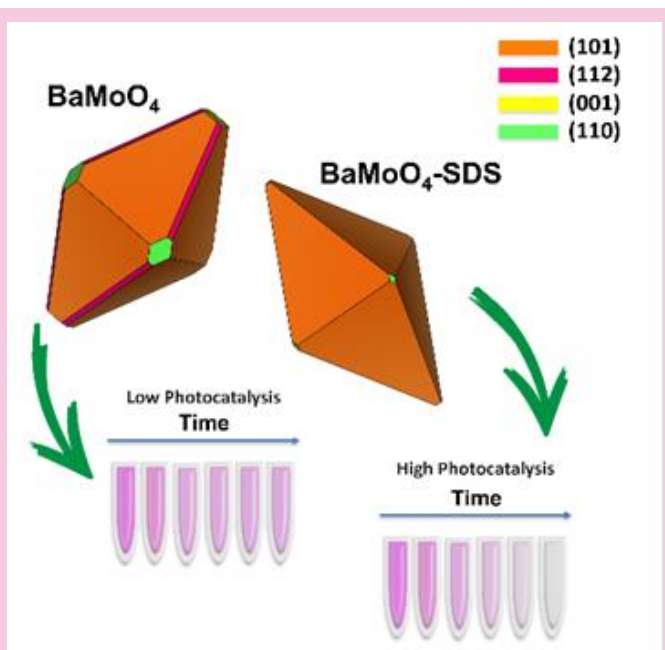
Published: April 11, 2022

Keywords:

1. DFT calculations
2. Rational design of materials
3. Barium molybdate
4. Surfactant-mediated morphology
5. Photocatalytic activity

Section Editors: Elson Longo and Juan Manuel Andrés Bort

ABSTRACT: This paper discloses the effect of the surfactant sodium dodecyl sulfate (SDS) in the morphology and the photocatalytic activity of BaMoO₄ crystals. Experimental techniques were applied to study the order-disorder degree of the samples. First-principles calculations were performed at density functional theory level with the B3LYP hybrid functional. The morphologies were investigated by field emission scanning electron microscopy, and the theoretical crystal shapes were obtained through the Wulff construction. The photocatalytic activity efficiency of the BaMoO₄ crystals was tested against the Rhodamine B (RhB) dye. In this paper, BaMoO₄ synthesized with SDS by the coprecipitation method presented a monophasic crystal with a disordered structure. In addition, the presence of this surfactant generated pores on the surfaces of the material, and those pores were responsible for the appearance of the adsorptive ability enhancing the adsorption process of the RhB dye in the dark, in absence of ultraviolet light.



1. Introduction

In past years, the ceramic's powders and crystals of molybdates were prepared by different methods, such as solid-state reaction (Kumar *et al.*, 2020), precipitation with calcination in high temperatures (Silva *et al.*, 2020), and the crystal growth by the "Czochralski" process (Khan *et al.*, 2020). However, these synthesis methods require high temperatures, long processing times, sophisticated equipment with high maintenance costs and can even lead to the formation of undesirable phases. Therefore, some synthesis methods have been developed and used in the preparation of molybdate crystals (Lakhlifi *et al.*, 2020; Skutina *et al.*, 2021; Tang *et al.*, 2021), such as coprecipitation (Chankhanittha *et al.*, 2021; F. Oliveira *et al.*, 2021), conventional hydrothermal (Farahpour and Arvand, 2021), microwave assisted hydrothermal (Keshari and Dubey, 2021), and sonochemical (Silva Junior *et al.*, 2021). These methods make possible to allay the problems present in older methods and obtain crystals of different sizes and shapes.

In particular, the coprecipitation method, which, according to the literature, is defined as a process for obtaining crystalline materials from the dissolution of reagents or soluble precursors in aqueous solution with or without the presence of a mineralizer (chemical bases) at relatively low temperature, has been used recently in the preparation of different molybdates of different shapes and sizes (Theiss *et al.*, 2016). However, to obtain homogeneous and monophasic molybdate crystals by this method, higher temperatures (> 100 °C) are necessary due to the low reaction kinetics (Kianpour *et al.*, 2013). Studies have been carried out using the coprecipitation method, employing surfactants as stabilizing agents to aid in the kinetics and, thus, reduce the reaction temperature (Kianpour *et al.*, 2016). These surfactants act as reactants during the reaction and stabilize the colloids. The literature also shows the effect of different surfactant ratios in controlling the size of microstructures and improving photocatalytic, photoluminescent, and antibacterial properties (Ji *et al.*, 2020; Keerthana *et al.*, 2021; Ray *et al.*, 2018). Among the used surfactants, the anionic sodium dodecyl sulphate (SDS) acts as a stabilizer protecting the newly formed cation or anion nuclei, which has an intrinsic preference for the growth of their crystals (Kianpour *et al.*, 2013; Luo *et al.*, 2010).

Among molybdates, barium molybdate (BaMoO_4) is relevant material in electro-optics due to its green luminosity production and electro-optic applications, including solid-state lasers and optical fibers. The BaMoO_4 presents a scheelite structure with $I4_1/a$ space

group formed by distorted $[\text{BaO}_8]$ and $[\text{MoO}_4]$ clusters. This material has a high band gap energy (E_{gap}) ~ 4.2 eV (Pereira *et al.*, 2021; Sczancoski *et al.*, 2010; Xia and Chen, 2010). Due to its poor use of light (ultraviolet [UV] light) from the solar spectrum, the photocatalytic efficiency becomes very low. Various techniques have been applied to photogenerate electron-hole pairs in semiconductors to improve photocatalytic performance, such as modeling new crystals through BaMoO_4 synthesis to form new morphologies efficient in enhancing the photocatalytic performance of BaMoO_4 (Hu *et al.*, 2021; Luo *et al.*, 2008; Xia and Chen, 2010). It is possible to correlate the size of materials with different or even new properties; thus, semiconductors designed with different sizes and exposed facets proved to be excellent models to promote, for example, photocatalytic and biocide studies (Macedo *et al.*, 2018).

This paper presents a simple method for the synthesis of uniform and pure BaMoO_4 crystals through the coprecipitation method using the SDS to evaluate the effects on the crystal morphology in the application of Rhodamine B (RhB) degradation. Thus, to endorse the experimental results, first-principles calculations were used to assess the effects of morphology on the degrading processes of the RhB.

2. Experimental sections

2.1 Synthesis

The BaMoO_4 crystals were synthesized by a simple coprecipitation method by using barium nitrate ($\text{Ba}(\text{NO}_3)_2$, Sigma-Aldrich, 99.0%), sodium molybdate dihydrate ($\text{NaMoO}_4 \cdot 2\text{H}_2\text{O}$, Sigma-Aldrich, 99.0%) as precursors, and the sodium dodecyl sulfate (SDS, Synth, 90.0%) as a surfactant. The first step of the synthesis involves the dissolution of 1×10^{-3} mol of the precursor's salts, separately, in 100 mL of deionized water at 70 °C. Then, 1 g of the surfactant SDS was added to the MoO_4^{2-} ions solution. After these steps, the two solutions were mixed under constant stirring. Approximately ten washes with deionized water were carried out at the end, using a centrifugation process (Centrifuge 5804, Eppendorf) to remove the residual Na^+ and organic ions. The synthesized solid was collected and dried in an oven at 65 °C for 24 h. The same procedure described above was repeated to obtain the pure BaMoO_4 crystal by removing the SDS in the precursor solution. The samples were named by BaMoO_4 and BaMoO_4 -SDS for the synthesis without and with SDS, respectively.

2.2 Structural and morphological characterization

The structure of BaMoO₄ crystals was characterized by X-ray diffraction (XRD) with Rietveld and micro-Raman. The morphological change was analyzed through field emission-scanning electron microscopy (FE-SEM), and the electronic modifications were analyzed by UV-visible (UV-vis) spectroscopy.

2.3 Photocatalysis evaluation

To analyze the surfactant's effect in the photocatalytic activity of the BaMoO₄ and BaMoO₄-SDS crystals, it was performed the photodegradation of the RhB (95%, Mallinckrodt) under UV light. The experiment was conducted as follows: 50.0 mL of RhB solution (1×10^{-5} mol L⁻¹) were added to the glass reactor with 50 mg of the sample. The reactor was taken to ultrasound (42 kHz, model 1510) for 5 min in the dark to disperse the BaMoO₄ crystals in the solution and then transferred to the photocatalytic system with 6 UV lamps (TUV Phillips, 15 W, and intensity of 254 nm), in 10 cm from the reactor. Then, to reach the adsorption equilibrium, the system remained in the dark for 40 min (collecting aliquots at -40, -30, -20, -10 and 0 min) at 25 °C and in the next step, the lamps were turned on, and the aliquots were removed at 20, 40, 60, 80, 110 and 140 min. After the reaction, the photocatalytic system was placed in a plastic tube where they were centrifuged at 10,000 rpm for 5 min to remove the catalyst particles from the solution completely. The remaining solution was analyzed by UV-vis absorption spectroscopy in a V-660 spectrophotometer (JASCO). The monitoring of the variation in the RhB absorption band with maximum $\lambda = 554$ nm for photocatalytic tests was investigated.

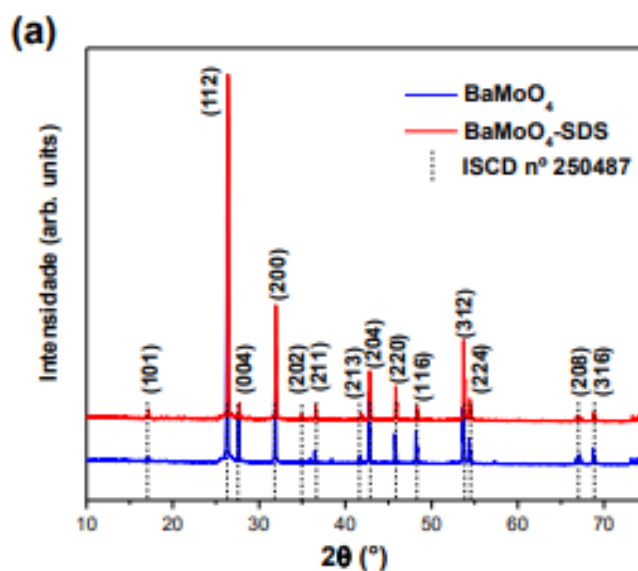
2.4 Theoretical models

First-principles calculations were performed using the CRYSTAL program (Dovesi *et al.*, 2017; 2018) at the DFT level associated with the B3LYP hybrid functional (Becke, 1988; 1993). To study the electronic properties of the BaMoO₄ structure, a unit cell model was created from the refinement data. In the optimization process to obtain the perfect crystal data, without defects, the lattice parameters (a , b , c , and α , β , γ) and the internal coordinates (x , y , z) of each atom were optimized. The electronic band gap energy (E_{gap}) value and the Raman frequencies were computed and compared with the experimental values. From the

calculated surface energy (E_{surf}) values published in the literature (M. Oliveira *et al.*, 2016), associated with the Wulff's construction, it was possible to obtain the ideal theoretical morphology (in vacuum) for the material studied. In addition to this ideal morphology and using the methodology developed by us (Andrés *et al.*, 2015), it was also possible to obtain the experimental morphology in order to compare it with the theoretical one.

3. Results and discussion

The XRD and Rietveld refinement was performed to verify the crystallinity of the material and its phase and structural parameters, as illustrated in Fig. 1. The XRD data allowed an analysis of the material structure at long-distance. It was possible to index and prove that both materials were obtained in their pure phase. As can be seen in Fig. 1a, it was not observed the presence of secondary phases, since the diffraction peaks are in good agreement with those reported for BaMoO₄ in ICSD n° 250487 (Inorganic Crystal Structure Database, ICSD) and the strong and acute peaks indicate that the synthesized crystals have good crystallinity. Structural refinement was performed using the Rietveld method for BaMoO₄ and BaMoO₄-SDS crystals to confirm that the structures belong to the tetragonal structure and obtain the lattice parameters, cell volume, and atomic coordinates (Fig. 1b). The structural refinement's quality was analyzed using the R_{wp} , R_{Bragg} , R_p e χ^2 statics parameters. Minor deviations of these parameters indicate the excellent quality of the structural refinement.



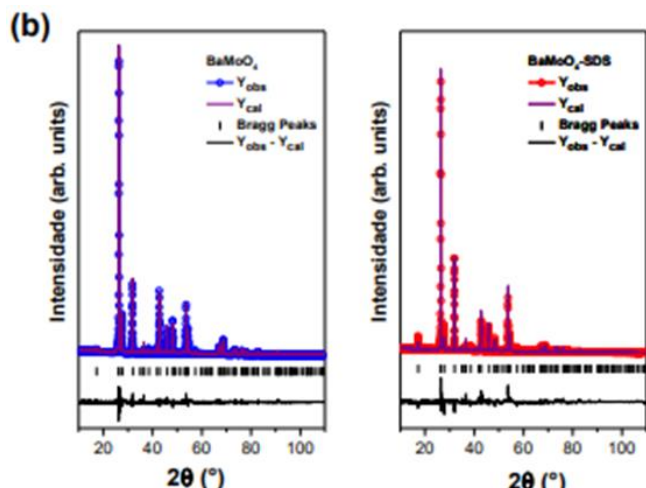


Figure 1. (a) X-ray diffraction patterns and (b) Rietveld refinement for BaMoO₄ crystals in the presence and absence of SDS.

The BaMoO₄ crystals, synthesized by the coprecipitation method with and without SDS, were obtained in their pure tetragonal phase (space group *I4₁/a*). Fig. 2 illustrates the tetragonal BaMoO₄ structure obtained from the refinement data. The crystal lattice of this semiconductor is formed by delta-hedral [BaO₈] and tetrahedral [MoO₄] clusters and contains four formula units per unit cell (*Z* = 4).

The analysis of the structural order/disorder degree of the BaMoO₄ crystals at a short distance was analyzed using the micro-Raman spectra. The results can be found in Fig. 3 and in Tab. 1, compared with the theoretical modes.

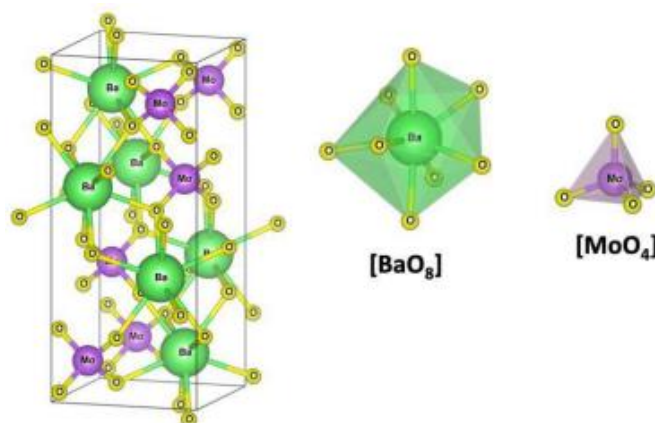


Figure 2. Tetragonal structure of BaMoO₄ and its constituent [BaO₈] and [MoO₄] clusters.

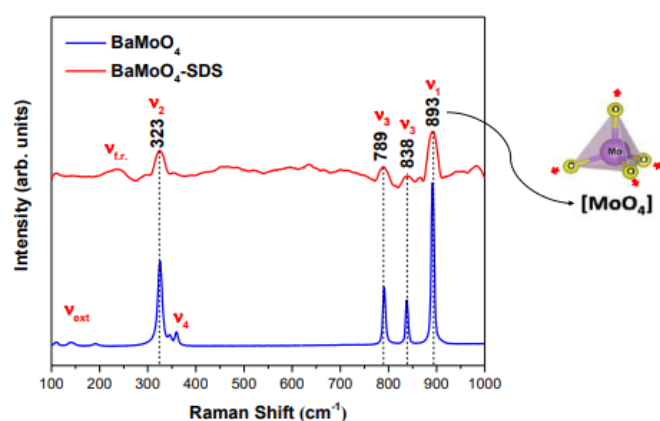


Figure 3. Micro-Raman spectroscopy for BaMoO₄ crystals in the presence and absence of SDS.

Table 1. Vibrational modes and Raman peaks of BaMoO₄ and theoretical values.

Vibrational modes and symmetry		Raman peaks (cm ⁻¹)		
Td	Lattice mode C ⁶ 4h	BaMoO ₄	BaMoO ₄ -SDS	BaMoO ₄ -Theo
ν ₁ (2A ₁)	A _g	893	893	907.95
ν ₃ (2F ₂)	B _g	838	838	853.78
ν ₃ (2F ₂)	E _g	789	789	818.28
ν ₄ (2F ₂)	E _g	360	-	367.90
ν ₄ (2F ₂)	B _g	345	-	366.19
ν ₂ (2E)	B _g , A _g	323	323	332.70
ν _{f,r} * (2F ₁)	E _g	-	238	212.10
ν _{ext} **	B _g	191	-	137.02
ν _{ext} **	E _g	142	-	122.86
ν _{ext} **	B _g , E _g	112	-	80.49

*Free rotation; **external modes.

As can be seen, the Raman bands related to the four active modes were observed. The vibrational modes observed in the Raman spectra are divided into two groups: the internal and external modes. The external

vibrational modes are composed of tetrahedral [MoO₄] clusters with strong covalent bonds between Mo–O and octahedral [BaO₈] clusters (Christofilos *et al.*, 2004; Sczancoski *et al.*, 2010). The internal modes are

composed of tetrahedral $[\text{MoO}_4]$ clusters with a rigid center of mass. The external modes can be considered as reticulated phonons because they result from the movement of $[\text{BaO}_8]$ and $[\text{MoO}_4]$ clusters, in symmetry T_d , in the free space generated (Panchal *et al.*, 2006). The BaMoO_4 samples exhibited all the internal and external modes, corresponding to the material's phase, well defined, indicating that the material is highly crystalline at close range. On the other hand, the Raman spectrum of $\text{BaMoO}_4\text{-SDS}$ showed peaks at 893, 838, 789, and 323 cm^{-1} , showing only the internal modes, demonstrating that this material is partially disordered. In addition, the $\text{BaMoO}_4\text{-SDS}$ has peaks corresponding to the internal modes, with less intensity, which is a characteristic for disordered crystals: the appearance of wide Raman bands reflecting on the density of the phonon states. These Raman results prove that the use of SDS in BaMoO_4 synthesis causes changes in the crystal structure at a short distance and that even with the pure BaMoO_4 phase confirmed by XRD results, these crystals are disordered.

The UV-vis spectra for the BaMoO_4 and $\text{BaMoO}_4\text{-SDS}$ samples made it possible to determine each E_{gap} value, applying the Kubelka–Munk function. This function is generally applied to convert diffuse reflectance into equivalent absorption coefficient and is mainly used to analyze powder samples and is described as (Eq. 1) (Wood and Tauc, 1972):

$$\alpha = F(R) = \frac{(1-R)^2}{2R} \quad (1)$$

where $F(R)$ is Kubelka-Munk function; α is the absorption coefficient, and R is the reflectance. Therefore, the Tauc relation becomes (Eq. 2):

$$F(R) = hv = \alpha(hv - E_{\text{gap}})n \quad (2)$$

where $n = 0.5$ and 2 for direct and indirect transitions, respectively, resulting in direct and indirect band intervals (Spassky *et al.*, 2005). The graphs of $(F(R)hv)^2$ versus hv for all samples are shown in Fig. 4. The extrapolation of linear regions from these graphs to $F(R)hv^2 = 0$ gives the direct band gap values.

The E_{gap} values show a slight variation between the samples. The decrease in the E_{gap} value for the $\text{BaMoO}_4\text{-SDS}$ crystals can be attributed to a reduction in the local order degree, which may have been caused by the creation of new intermediate levels between the valence (VB) and conduction bands (CB). This fact can be attributed to the presence of the SDS surfactant during the synthesis of the material that causes

distortions in the crystal structure, which endorse the experimental Raman spectra.

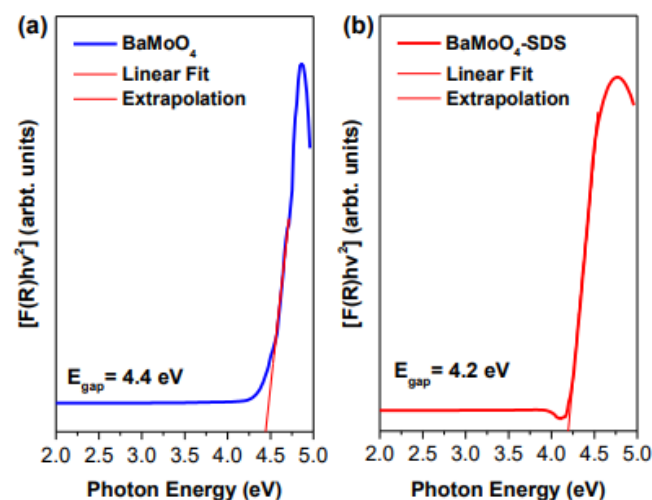
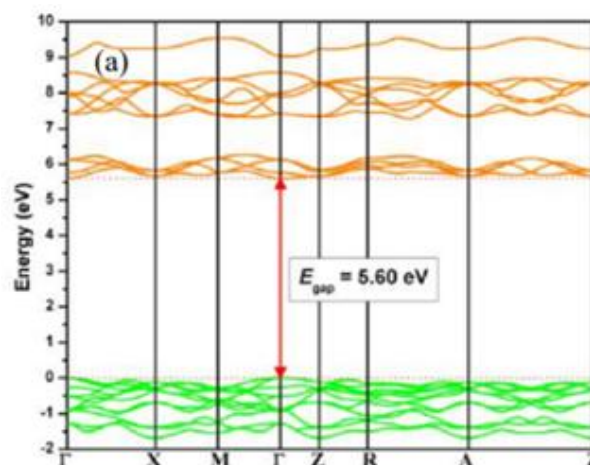


Figure 4. UV-vis spectra for the BaMoO_4 crystals in the presence and absence of SDS.

The theoretical study of the electronic properties corroborates with the UV-vis results. The theoretical model of the BaMoO_4 is seen as a defect-free structure with ideal parameters. This model presented a higher E_{gap} value (Fig. 5a) of 5.60 eV. The observed electronic transition is direct between the Γ -points of the Brillouin zone. The atomic composition of the VB and CB was investigated by analyzing the density of states (DOS) from all atoms in the structure. As shown in Fig. 5b, the VB for BaMoO_4 is mainly formed by the contribution of the orbitals from the O atoms, and these orbitals are mostly antibonding types. On the other hand, the CB is composed primarily by the hybridization of the orbitals from the Mo and O atoms. This region also has a contribution from the Ba atoms. There is the presence of bonding and antibonding orbitals.



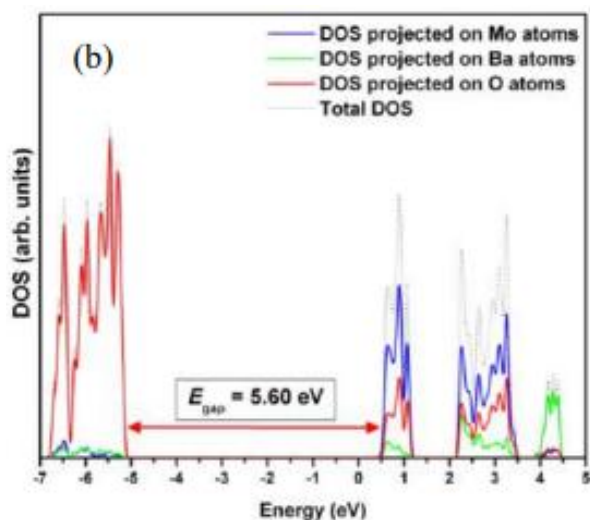


Figure 5. (a) Band structure and (b) Total and projected DOS for the BaMoO₄ structure.

The morphologies of the BaMoO₄ and BaMoO₄-SDS crystals were investigated by microscopy, and the FE-SEM images are illustrated in Fig. 6. The BaMoO₄

crystals synthesized without the surfactant present an octahedron-shaped morphology with a predominance of the (101) surface, with a small contribution of the (112) and (110) surfaces (Fig. 6a). Better visualization of these surfaces can be seen in the theoretical morphology known as Wulff's crystal. To achieve this theoretical morphology, it was employed the methodology developed by Andrés *et al.* (2015), in which used the calculated surface energy (E_{surf}) values associated with the Wulff construction (Wulff, 1901). The E_{surf} of the BaMoO₄ crystals were reported by M. Oliveira *et al.* (2016). The morphology observed for the crystals obtained in the presence of SDS (Fig. 6b) presents the same crystal shape as the sample without SDS (Fig. 6a). However, morphological differences are observed, such as the (112) surface no longer contributes to the morphology of the crystal, and the (110) starts to have a minor contribution. The major difference between the morphologies of BaMoO₄ and BaMoO₄-SDS is in the shape texture. BaMoO₄-SDS crystals have a rugged surface with the presence of pores.

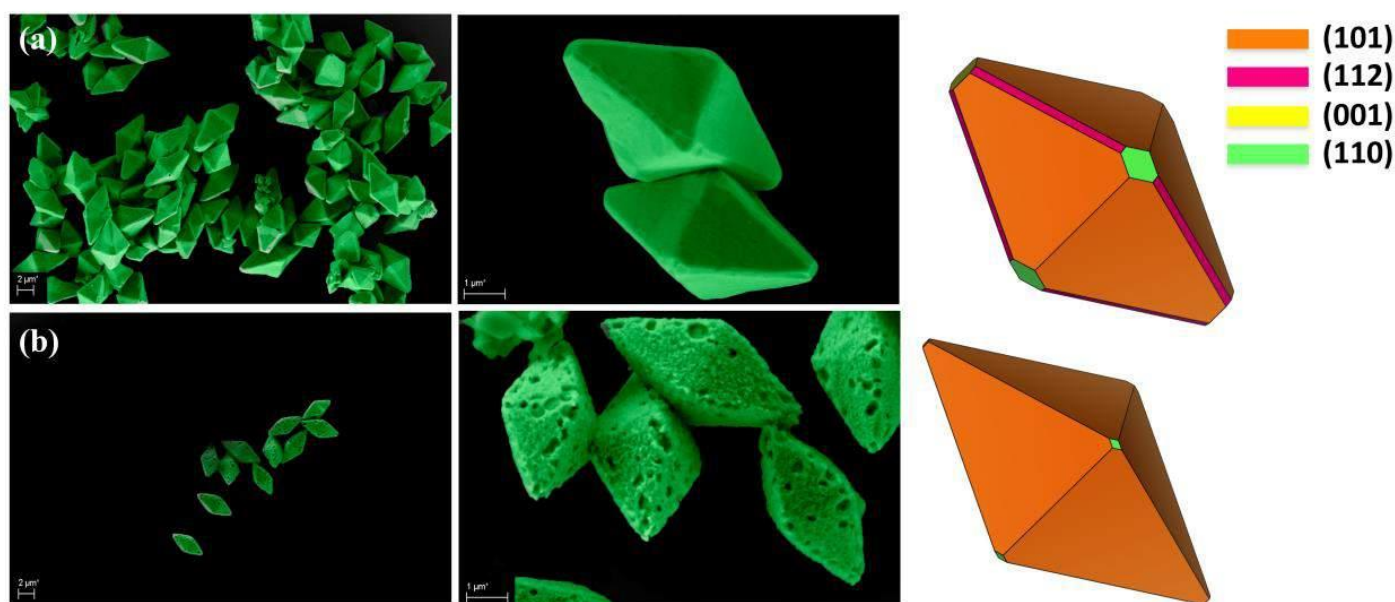


Figure 6. FE-SEM images for the (a) BaMoO₄ e (b) BaMoO₄-SDS crystals. For the comparison, Wulff's crystals are also represented for each sample.

M. Oliveira *et al.* (2016) reported the synthesized of the BaMoO₄ crystals also by the coprecipitation method; however, they used a temperature of 80 °C, at pH 7. They modeled the BaMoO₄ surfaces and calculated the surface energies. The morphology reported by the authors is different from that obtained in this study, with a significant presence of the (100), (112), (110), and (101) surfaces. Through these results, it is possible to

observe that the surfaces of this BaMoO₄ structure present, mainly, different types of clusters for the Ba atom, with several oxygen vacancies.

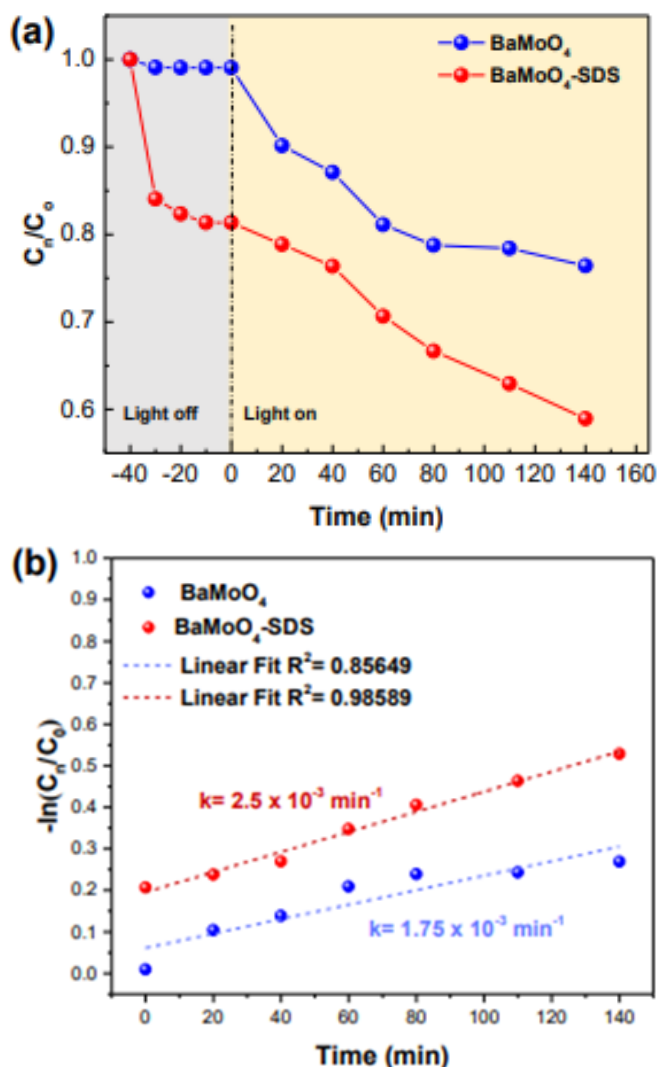


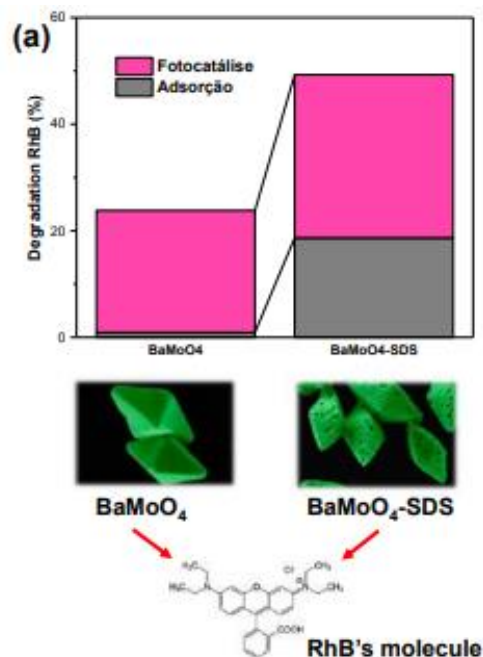
Figure 7. (a) Photocatalysis degradation profile of the RhB dye in 140 min and (b) first-order kinetics for the $BaMoO_4$ crystals in the presence and absence of SDS.

The photocatalytic activity of the $BaMoO_4$ crystals was tested against the RhB dye. The analysis started in the dark (light off) to test the influence of this environment in the photocatalysis process and obtain the adsorptive equilibrium. The equilibrium adsorption-desorption rate of RhB in the dark versus time in the presence of $BaMoO_4$ and $BaMoO_4$ -SDS was shown in Fig. 7a and Fig. 8a. The $BaMoO_4$ -SDS degradation profiles in the dark showed that this material has one more property that has not yet been reported in the literature, the adsorptive capacity. The $BaMoO_4$ -SDS crystals adsorbed about 18% of RhB while $BaMoO_4$ adsorbed about 1% of RhB. This property is acquired by the presence of pores in the crystal surfaces (see FE-SEM images in Fig. 6a), as illustrated in Fig. 8b. The high roughness of this material confers such properties,

and the adsorptive process added to the photocatalytic process certainly makes the material promising in the studies of adsorptive and photocatalysis processes. These two properties were illustrated in Fig. 8b–c. In addition, the $BaMoO_4$ -SDS also has a photocatalytic performance enhancement, as seen in Fig. 7b.

Therefore, by analyzing the degradation profile shown in Fig. 7a, it can be seen that the presence of SDS in the synthesis improved the photocatalytic activity. $BaMoO_4$ crystals degraded about 23% in 140 min, while the degradation of the $BaMoO_4$ -SDS crystals was 45%. The process analysis showed that both degradations occur in first-order kinetics. The calculated velocity constants were $k = 1.75 \times 10^{-3} \text{ min}^{-1}$ and $k = 2.50 \times 10^{-3} \text{ min}^{-1}$ for the $BaMoO_4$ and $BaMoO_4$ -SDS crystals, respectively, as shown in Fig. 7b. So, the increase in reaction kinetics indicates that $BaMoO_4$ synthesis in the presence of SDS is favorable for materials with photocatalytic properties.

Hence, the control of morphology is of fundamental importance because the properties of the materials depend on the kind of surfaces that constitute their morphology. In the case of the $BaMoO_4$ crystal, the use of the SDS favored the increase of the (101) surface and caused deformations on the crystal surfaces, considerably altering the morphology. This change is mainly responsible for creating and improving the main properties of the $BaMoO_4$ crystals studied in this work.



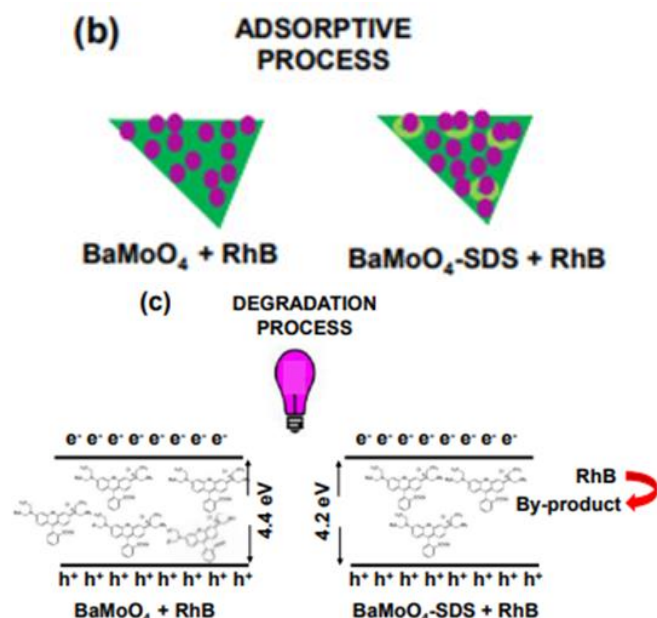


Figure 8. (a) Photocatalysis and adsorptive degradation of the RhB dye. (b) The mechanism proposed for the adsorptive process and (c) degradation process at the BaMoO₄ surfaces on the morphology obtained in the presence and absence of SDS.

4. Conclusions

In this study, it was possible to understand how the presence of a surfactant, in this case, the SDS, can generate changes in the morphology of the BaMoO₄ crystals and how this fact shifts the photocatalytic activity. In the case of BaMoO₄ synthesized with SDS, the presence of this surfactant generated pores on the surface of the material's morphology, and the presence of these pores facilitated the adsorption process of the RhB dye in the dark, without the presence of UV light, and, consequently, a new property for that semiconductor was created, the adsorptive capacity. In addition to the acquired adsorptive ability, BaMoO₄ synthesized with SDS showed a photocatalytic improvement. These results demonstrate that morphology control can influence the creation of new properties, opening a range of opportunities for further studies.

Authors' contribution

Conceptualization: Gouveia, A. F.; Bellucci, G. V.; Ribeiro, L. R.; Assis, M.

Data curation: Gouveia, A. F.; Bellucci, G. V.; Ribeiro, L. R.

Formal Analysis: Gouveia, A. F.; Bellucci, G. V.; Ribeiro, L. R.; Assis, M.

Funding acquisition: Gouveia, A. F.; Bellucci, G. V.; Ribeiro, L. R.; Assis, M.; Rosa, I. L. V.; Longo, E.; Andrés, J.; San-Miguel, M. A.

Investigation: Gouveia, A. F.; Bellucci, G. V.; Ribeiro, L. R.; Assis, M.; Rosa, I. L. V.; Longo, E.; Andrés, J.; San-Miguel, M. A.

Methodology: Gouveia, A. F.; Bellucci, G. V.; Ribeiro, L. R.; Assis, M.

Project administration: Gouveia, A. F.; Ribeiro, L. R.; Longo, E.; Andrés, J.; San-Miguel, M. A.

Resources: Gouveia, A. F.; Longo, E.; Andrés, J.; San-Miguel, M. A.

Software: Gouveia, A. F.; Andrés, J.; San-Miguel, M. A.

Supervision: I. L. V.; Longo, E.; Andrés, J.; San-Miguel, M. A.

Validation: Gouveia, A. F.; Bellucci, G. V.; Ribeiro, L. R.; Assis, M.; Rosa, I. L. V.; Longo, E.; Andrés, J.; San-Miguel, M. A.

Visualization: Gouveia, A. F.; Bellucci, G. V.; Ribeiro, L. R.; Assis, M.; Rosa, I. L. V.; Longo, E.; Andrés, J.; San-Miguel, M. A.

Writing – original draft: Gouveia, A. F.; Ribeiro, L. R.

Writing – review & editing: Gouveia, A. F.; Ribeiro, L. R.; Longo, E.; Andrés, J.; San-Miguel, M. A.

Data availability statement

The data will be available upon request. All data sets were generated or analyzed in the current study.

Funding

Fundação de Amparo à Pesquisa do Estado de São Paulo (FAPESP), <https://doi.org/10.13039/501100001807>. Grant No: 2013/07296-2; 2016/23891-6; 2017/26105-4; 2019/01732-1.

Financiadora de Estudos e Projetos, <https://doi.org/10.13039/501100004809>.

Conselho Nacional de Desenvolvimento Científico e Tecnológico (CNPq), <https://doi.org/10.13039/501100003593>. Grant No: 166281/2017-4; 305792/2020-2.

Generalitat Valenciana, <https://doi.org/10.13039/501100003359>. Grant No: BEST/2021/048.

Acknowledgments

This work used computational resources of the “Centro Nacional de Processamento de Alto Desempenho em São Paulo” (CENAPAD-SP), “Centro de Computação John David Rogers” (CCJDR-UNICAMP), and the CENAPAD-RJ (SDumont) and used experimental resources from Centro de Desenvolvimento de Materiais Funcionais (CDMF). A.F.G acknowledges the Universitat Jaume I for the postdoctoral contract (POSDOC/2019/30), FAPESP for the postdoctoral fellowship and Generalitat Valenciana for the exterior research grant. J.A. acknowledges Universitat Jaume I (project UJI-B2019-30), and the Ministerio de Ciencia, Innovación y Universidades (Spain) (project PGC2018094417-B-I00) for financially supporting this research.

References

- Andrés, J.; Gracia, L.; Gouveia, A. F.; Ferrer, M. M.; Longo, E. Effects of surface stability on the morphological transformation of metals and metal oxides as investigated by first-principles calculations. *Nanotechnology* **2015**, *26* (40), 405703. <https://doi.org/10.1088/0957-4484/26/40/405703>
- Becke, A. D. Density-Functional Exchange-Energy Approximation with Correct Asymptotic-Behavior. *Phys. Rev. A* **1988**, *38*, 3098–3100. <https://doi.org/10.1103/PhysRevA.38.3098>
- Becke, A. D. Density-Functional Thermochemistry .3. The Role of Exact Exchange. *J. Chem. Phys.* **1993**, *98*, 5648–5652. <https://doi.org/10.1063/1.464913>
- Chankhanittha, T.; Somaudon, V.; Watcharakitti, J.; Nanan, S. Solar light-driven photocatalyst based on bismuth molybdate (Bi₄MoO₉) for detoxification of anionic azo dyes in wastewater. *J. Mater. Sci.: Mater. Electron.* **2021**, *32*, 1977–1991. <https://doi.org/10.1007/s10854-020-04965-5>
- Christofilos, D.; Arvanitidis, J.; Kampasakali, E.; Papagelis, K.; Ves, S.; Kourouklis, G. A. High pressure Raman study of BaMoO₄. *Phys. Status Solidi B* **2004**, *241* (14), 3155–3160. <https://doi.org/10.1002/pssb.200405234>
- Dovesi, R.; Saunders, V. R.; Roetti, C.; Orlando, R.; Zicovich-Wilson, C. M.; Pascale, F.; Civalleri, B.; Doll, K.; Harrison, N. M.; Bush, I. J.; D'Arco, P.; Llunel, M.; Causà, M.; Noël, Y.; Maschio, L.; Erba, A.; Rerat, M.; Casassa, S. *CRYSTAL17 User's Manual*; University of Torino, 2017.
- Dovesi, R.; Erba, A.; Orlando, R.; Zicovich-Wilson, C. M.; Civalleri, B.; Maschio, L.; Rerat, M.; Casassa, S.; Baima, J.; Salustro, S.; Kirtman, B. Quantum-mechanical condensed matter simulations with CRYSTAL. *Wiley Interdiscip. Rev. Comput. Mol. Sci.* **2018**, *8* (4), e1360. <https://doi.org/10.1002/wcms.1360>
- Farahpour, M.; Arvand, M. Single-pot hydrothermal synthesis of copper molybdate nanosheet arrays as electrode materials for high areal-capacitance supercapacitor. *J. Energy Storage* **2021**, *40*, 102742. <https://doi.org/10.1016/j.est.2021.102742>
- Hu, X.; Jiang, S.; Fu, S.; Xie, J.; Zhong, L.; Chen, M.; Xiang, G.; Wang, Y.; Li, L.; Zhou, X. Opposite temperature luminescent behaviours of Tb³⁺ and Pr³⁺ co-doped BaMoO₄ glass ceramics for temperature sensing. *J. Lumin.* **2021**, *236*, 118080. <https://doi.org/10.1016/j.jlumin.2021.118080>
- Ji, T.; Ha, E.; Wu, M. Z.; Hu, X.; Wang, J.; Sun, Y. A.; Li, S. J.; Hu, J. Q. Controllable Hydrothermal Synthesis and Photocatalytic Performance of Bi₂MoO₆ Nano/Microstructures. *Catalysts* **2020**, *10*. <https://doi.org/10.3390/catal10101161>
- Keerthana, S. P.; Rani, B. J.; Yuvakkumar, R.; Ravi, G.; Shivatharsiny, Y.; Babu, E. S.; Almoallim, H. S.; Alharbi, S. A.; Velauthapillai, D. Copper molybdate nanoparticles for electrochemical water splitting application. *Int. J. Hydrogen Energy* **2021**, *46* (11), 7701–7711. <https://doi.org/10.1016/j.ijhydene.2020.12.029>
- Keshari, A. S.; Dubey, P. Rapid microwave-assisted vs. hydrothermal synthesis of hierarchical sheet-like NiO/NiMoO₄ hybrid nanostructures for high performance extrinsic pseudocapacitor application. *J. Energy Storage* **2021**, *40*, 102629. <https://doi.org/10.1016/j.est.2021.102629>
- Khan, A.; Daniel, J.; Tyagi, M.; Kim, H. J.; Lee, M. H.; Kim, Y. Czochralski growth, electronic structure, luminescence and scintillation properties of Cs₂Mo₃O₁₀: A new scintillation crystal for 0νββ decay search. *J. Alloys Compd.* **2020**, *821*, 153466. <https://doi.org/10.1016/j.jallcom.2019.153466>
- Kianpour, G.; Salavati-Niasari, M.; Emadi, H. Precipitation synthesis and characterization of cobalt molybdates nanostructures. *Superlattices Microstruct.* **2013**, *58*, 120–129. <https://doi.org/10.1016/j.spmi.2013.01.014>
- Kianpour, G.; Soofivand, F.; Badieli, M.; Salavati-Niasari, M.; Hamadani, M. Facile synthesis and characterization of nickel molybdate nanorods as an effective photocatalyst by co-precipitation method. *J. Mater. Sci.: Mater. Electron.* **2016**, *27*, 10244–10251. <https://doi.org/10.1007/s10854-016-5103-3>
- Kumar, V.; Chen, J.; Li, S.; Matz, S.; Bhavanasi, V.; Parida, K.; Al-Shamery, K.; Lee, P. S. Tri-rutile layered niobium-molybdates for all solid-state symmetric supercapacitors. *J. Mater. Chem. A* **2020**, *8* (38), 20141–20150. <https://doi.org/10.1039/D0TA03678A>
- Lakhlifi, H.; El Jabbar, Y.; El Ouati, R.; Er-Rakho, L.; Durand, B.; Guillemet-Fritsch, S. Synthesis of molybdates

- Zn_{1-x}Co_xMoO₄ (0 ≤ x ≤ 1), by decomposition of the precursors developed by the glycine-nitrate process (GNP), and their characterization. *Mater. Sci. Semicon. Proc.* **2020**, *114*, 105054. <https://doi.org/10.1016/j.mssp.2020.105054>
- Luo, Z.; Li, H.; Shu, H.; Wang, K.; Xia, J.; Yan, Y. Synthesis of BaMoO₄ Nestlike Nanostructures Under a New Growth Mechanism. *Cryst. Growth Des.* **2008**, *8* (7), 2275–2281. <https://doi.org/10.1021/cg700967y>
- Luo, Y.-S.; Dai, X.-J.; Zhang, W.-D.; Yang, Y.; Sun, C. Q.; Fu, S.-Y. Controllable synthesis and luminescent properties of novel erythrocyte-like CaMoO₄ hierarchical nanostructures via a simple surfactant-free hydrothermal route. *Dalton Trans.* **2010**, *39* (9), 2226–2231. <https://doi.org/10.1039/B915099D>
- Macedo, N. G.; Gouveia, A. F.; Roca, R. A.; Assis, M.; Gracia, L.; Andrés, J.; Leite, E. R.; Longo, E. Surfactant-Mediated Morphology and Photocatalytic Activity of α-Ag₂WO₄ Material. *J. Phys. Chem. C* **2018**, *122* (15), 8667–8679. <https://doi.org/10.1021/acs.jpcc.8b01898>
- Oliveira, M. C.; Gracia, L.; Nogueira, I. C.; Gurgel, M. F. C.; Mercury, J. M. R.; Longo, E.; Andres, J. On the morphology of BaMoO₄ crystals: A theoretical and experimental approach. *Cryst. Res. Technol.* **2016**, *51* (10), 634–644. <https://doi.org/10.1002/crat.201600227>
- Oliveira, F. K. F.; Santiago, A. A. G.; Catto, A. C.; Silva, L. F.; Tranquilin, R. L.; Longo, E.; Motta, F. V.; Bomio, M. R. D. Cerium molybdate nanocrystals: Microstructural, optical and gas-sensing properties. *J. Alloys Compd.* **2021**, *857*, 157562. <https://doi.org/10.1016/j.jallcom.2020.157562>
- Panchal, V.; Garg, N.; Sharma, S. M. Raman and x-ray diffraction investigations on BaMoO₄ under high pressures. *J. Phys.: Condens. Matter* **2006**, *18* (16), 3917. <https://doi.org/10.1088/0953-8984/18/16/002>
- Pereira, W. S.; Sczancoski, J. C.; Longo, E. Tailoring the photoluminescence of BaMoO₄ and BaWO₄ hierarchical architectures via precipitation induced by a fast precursor injection. *Mater. Lett.* **2021**, *293*, 129681. <https://doi.org/10.1016/j.matlet.2021.129681>
- Ray, S. K.; Dhakal, D.; Regmi, C.; Yamaguchi, T.; Lee, S. W. Inactivation of *Staphylococcus aureus* in visible light by morphology tuned α-NiMoO₄. *J. Photochem. Photobiol. A* **2018**, *350*, 59–68. <https://doi.org/10.1016/j.jphotochem.2017.09.042>
- Sczancoski, J. C.; Cavalcante, L. S.; Marana, N. L.; Silva, R. O.; Tranquilin, R. L.; Joya, M. R.; Pizani, P. S.; Varela, J. A.; Sambrano, J. R.; Li, M. S.; Longo, E.; Andres, J. *Curr. Appl. Phys.* **2010**, *10* (2), 614–624. <https://doi.org/10.1016/j.cap.2009.08.006>
- Silva Junior, J. L.; Nobre, F. X.; Freitas, F. A.; Carvalho, T. A. F.; Barros, S. S.; Nascimento, M. C.; Manzato, L.; Matos, J. M. E.; Brito, W. R.; Leyet, Y.; Couceiro, P. R. C. Copper molybdate synthesized by sonochemistry route at room temperature as an efficient solid catalyst for esterification of oleic acid. *Ultrason. Sonochem.* **2021**, *73*, 105541. <https://doi.org/10.1016/j.ultsonch.2021.105541>
- Silva, M. V.; Oliveira, D. F. M.; Oliveira, H. S.; Siqueira, K. P. F. Influence of temperature on the structural and color properties of nickel molybdates. *Mater. Res. Bull.* **2020**, *122*, 110665. <https://doi.org/10.1016/j.materresbull.2019.110665>
- Skutina, L.; Filonova, E.; Medvedev, D.; Maignan, A. Undoped Sr₂MMoO₆ Double Perovskite Molybdates (M = Ni, Mg, Fe) as Promising Anode Materials for Solid Oxide Fuel Cells. *Materials* **2021**, *14* (7), 1715. <https://doi.org/10.3390/ma14071715>
- Spassky, D.; Ivanov, S.; Kitaeva, I.; Kolobanov, V.; Mikhailin, V.; Ivleva, L.; Voronina, I. Optical and luminescent properties of a series of molybdate single crystals of scheelite crystal structure. *Phys. Status Solidi C* **2005**, *2* (1), 65–68. <https://doi.org/10.1002/pssc.200460112>
- Tang, C.; Wang, H.; Hong, Y.; Xu, W.; Shi, Q.; Liu, Z. Roughness induced wettability amplification of novel copper molybdate-branched CuO nanorod arrays by non-aqueous solution method. *Mater. Lett.* **2021**, *300*, 130260. <https://doi.org/10.1016/j.matlet.2021.130260>
- Theiss, F. L.; Ayoko, G. A.; Frost, R. L. Synthesis of layered double hydroxides containing Mg²⁺, Zn²⁺, Ca²⁺ and Al³⁺ layer cations by co-precipitation methods—A review. *Appl. Surf. Sci.* **2016**, *383*, 200–213. <https://doi.org/10.1016/j.apsusc.2016.04.150>
- Wood, D. L.; Tauc, J. Weak Absorption Tails in Amorphous Semiconductors. *Phys. Rev. B* **1972**, *5*, 3144. <https://doi.org/10.1103/PhysRevB.5.3144>
- Wulff, G. XXV. Zur Frage der Geschwindigkeit des Wachstums und der Auflösung der Krystallflächen. *Zeitschrift für Kristallographie - Crystalline Materials* **1901**, *34* (1–6). <https://doi.org/10.1524/zkri.1901.34.1.449>
- Xia, Z.; Chen, D. Synthesis and Luminescence Properties of BaMoO₄:Sm³⁺ Phosphors. *J. Am. Ceram. Soc.* **2010**, *93* (5), 1397–1401. <https://doi.org/10.1111/j.1551-2916.2009.03574.x>